



MEASUREMENT AND ANALYSIS OF MODULATED DOUBLET MODE RESPONSE IN MOCK BLADED DISKS

J. Y. CHANG AND J. A. WICKERT

*Department of Mechanical Engineering, Carnegie Mellon University, Pittsburgh,
PA 15213-3890, U.S.A.*

(Received 14 March 2001)

The steady state response of spatially modulated doublet modes that occur in low count flexible bladed disks is investigated for the case in which the structure is driven by a harmonic travelling wave excitation source. Finite-element simulation and modal testing of prototypical bladed-disk structures demonstrate the presence of particular wavenumbers, beyond the base number of nodal diameters, which contaminate and distort the appearance of certain doublet modes. The manner in which the natural frequency and wavenumber content of such modes shift and split as functions of the number of blades and their span angle is discussed in the light of a companion perturbation analysis for rotationally periodic structures. Resonance conditions are established and verified through simultaneous measurements made with a spin test stand using sensors that are placed in the rotating (structure) and stationary (excitation) frames of reference. The travelling wave response components of a repeated frequency doublet mode are shown to propagate either in the same or opposite direction as the excitation source, depending on whether certain algebraic relationships between the excitation order, the base number of nodal diameters, and the contamination wavenumbers are satisfied. To the extent that such components can travel at different phase speeds and directions relative to one another, the placement of sensors on the structure can be optimized to best measure the response amplitude. Conversely, other placements can result in submaximal measurement of peak vibration amplitude over the structure.

© 2002 Academic Press

1. INTRODUCTION

Engineering applications of rotationally periodic structures include turbines, automotive and aircraft braking systems, satellite antennae, clamping collars in computer disk drives, and the stator–rotor assemblies of electrical machinery. While these applications may be diverse, a common characteristic of such systems is that from the modelling perspective, an otherwise axisymmetric disk-like or shell-like structure is perturbed by the regular circumferential placement of geometric features, material variations, or other modifications. The natural frequencies, mode shapes, and overall structural behavior each change, and in particular, the response to a harmonic travelling wave excitation source exhibits features not otherwise present in the limit of axisymmetry.

In an axisymmetric structure, a doublet mode having repeated natural frequencies is denoted (m, n) , where m is the number of nodal circles and n is the number of nodal diameters. As periodic features would be gradually added, axisymmetry is lost, and the doublets are classified as being either repeated or split in frequency. Criteria for frequency splitting in slightly asymmetric or periodic structures have been developed through

a variety of analytical and experimental means [1–3]. Thomas [4, 5] and Ren and Zheng [6], developed finite-element formulations in which substructure-level models were used to describe dynamic response. Distorted mode shapes were reported by Wang and Williams [7] through their simulations and measurements of laminated electrical stators. Without developing a detailed classification of the natural frequency and mode structure, several experimental investigations have addressed mode shape visualization in bladed-disk structures [8] and cracked annular disks [9, 10]. By using both finite-element calculations and measurements, Ewins and Imregun [11] examined the shifting of natural frequencies and the distortion of mode shapes that occur in packeted bladed disks, where those shapes have wavenumber content in addition to the base number of nodal diameters. Analogous conclusions were reached by Fox *et al.* [12, 13] in their analysis of ring-like structure vibration. A criterion for predicting contamination wavenumber content was discussed by Kim *et al.* [14] in the context of point stiffness perturbations that were added to an otherwise axisymmetric distributed parameter system.

Modal expansion methods have primarily been used to understand steady state response in the presence of a harmonic travelling wave excitation source. In experimental and analytical analyses of imperfect or perturbed circular disks, the response has been described in terms of forward and backward waves which travel relative to an observer in the fixed reference frame [8, 15, 16]. Standing and travelling wave responses of bladed disks have also been examined through conventional frequency–speed analyses [17–22]. Wagner and Griffin [23, 24] examined the free and forced vibration of shrouded bladed disks with a view towards exploiting cyclic symmetry and increasing computational efficiency.

In what follows, the response of doublet modes to various order excitations, wherein each doublet can have substantial wavenumber content beyond a base number of nodal diameters, is examined through both simulations and measurements conducted with prototypical integral bladed disks. Emphasis is placed on the nature and implications of multiple propagating wave components being present in the bladed disk's response. The near-resonant behavior is discussed in the framework of the perturbation analysis developed in a companion paper [25]. In air impingement spin stand test, disk vibration measurements are made simultaneously in the stationary (excitation) and rotating (structure) reference frames, and the results are compared to model predictions made using finite element, modal testing, and perturbation analysis methods. Parameter studies in blade depth, blade span angle, and sensor location are discussed with a view to either detecting or reducing the peak response amplitude over the entire bladed-disk structure.

2. BLADED-DISK TEST STAND AND MEASUREMENT

As shown in Figures 1 and 2(a), experimental bladed disks of uniform thickness 0.5 mm and root radius $r_0 = 12.7$ cm were laser cut from annealed stainless-steel sheet stock. The disks had $NB = 4, 5,$ or 6 nominally identical sector-shaped blades, each of depth Δr and span angle α . The illustration of Figure 1 differs slightly from the test disks as 5 mm radius fillets were incorporated in the latter at each concave or convex corner. The disks were fixed around their inner periphery $r_i = 5.95$ cm by a clamping collar, and directly driven by a variable speed motor at speeds Ω to 2400 rev/min. These mock bladed disks preserve disk compliance, and they present significant coupling between the blades and the disk and between different blades. Those aspects of the forced response problem are of primary interest in this investigation. However, it should be noted that to the extent the disks are thin and planar, they do not model the aerodynamic properties of bladed disks as are present in the motivating applications discussed above. The entire test stand was bolted to

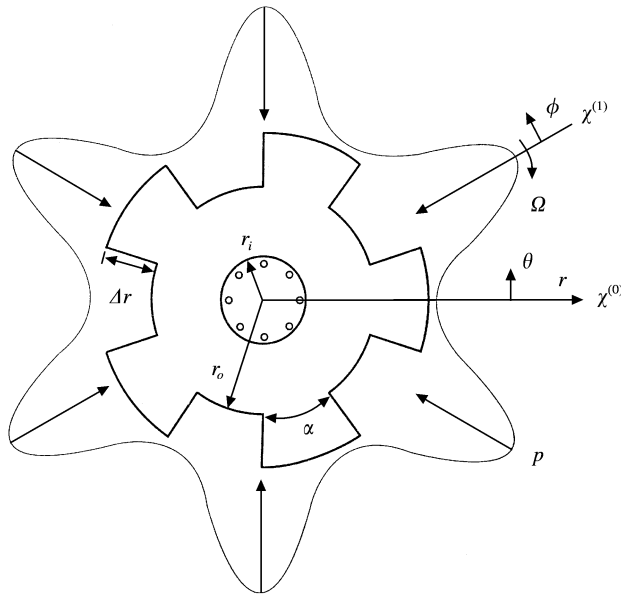


Figure 1. Schematic of a centrally clamped bladed disk structure with $NB = 5$ sector-shaped blades. The harmonic pressure source P in frame $\chi^{(1)}$ travels clockwise relative to the bladed disk's frame $\chi^{(0)}$.

a multi-ton granite table so as to eliminate vibration coupling with the environment, and for safety purposes, secured in a concrete and steel enclosure.

In the spin test stand of Figure 2(b), N evenly placed air jet nozzles were mounted on a stationary backing plate, which was parallel to the bladed disk but spaced 1.0 cm from it. The nozzles were located at common radius $r^* = 12.5$ cm, and each nozzle's outlet orifice of cross-sectional area $a = 0.03$ cm² was set some 5 mm from the spinning disk's surface. Constant air pressure was maintained in the supply manifold, and independent pressure regulators were adjusted to ensure uniformity of the nozzle flows, and to approximate a spatially harmonic pressure source that rotates relative to the disk.

The pressure field p applied to the disk in this manner was measured by using a manometer probe placed adjacent to the bladed disk at various stations ϕ around its circumference. The nozzles and regulators were adjusted in response to the pressure measurements so as to obtain a pressure field well-approximated by an N th harmonic in ϕ . A typical measurement of the pressure distribution near the disk's surface is depicted in Figure 3 for the case $N = 4$. The probe's readings (data points in Figure 3) were taken at 32 equally spaced stations. Nozzle flows were purposefully and iteratively adjusted in order to maintain a $P_0 = 30$ psi peak value at locations directly opposite each nozzle. The least-squares fit of the data to a cosine function, also shown in Figure 3, indicates the degree to which the experimental source is modelled as a harmonic function in the ground-based co-ordinate. Accordingly, with $\omega = N\Omega$ being the excitation frequency, the force-per-unit-area applied is approximated by

$$p(r, \theta) = \frac{aP_0}{2r} \delta(r - r^*) (1 + \cos(N\theta + \omega t)) \tag{1}$$

in terms of co-ordinate θ which rotates clockwise at speed Ω with the bladed disk.

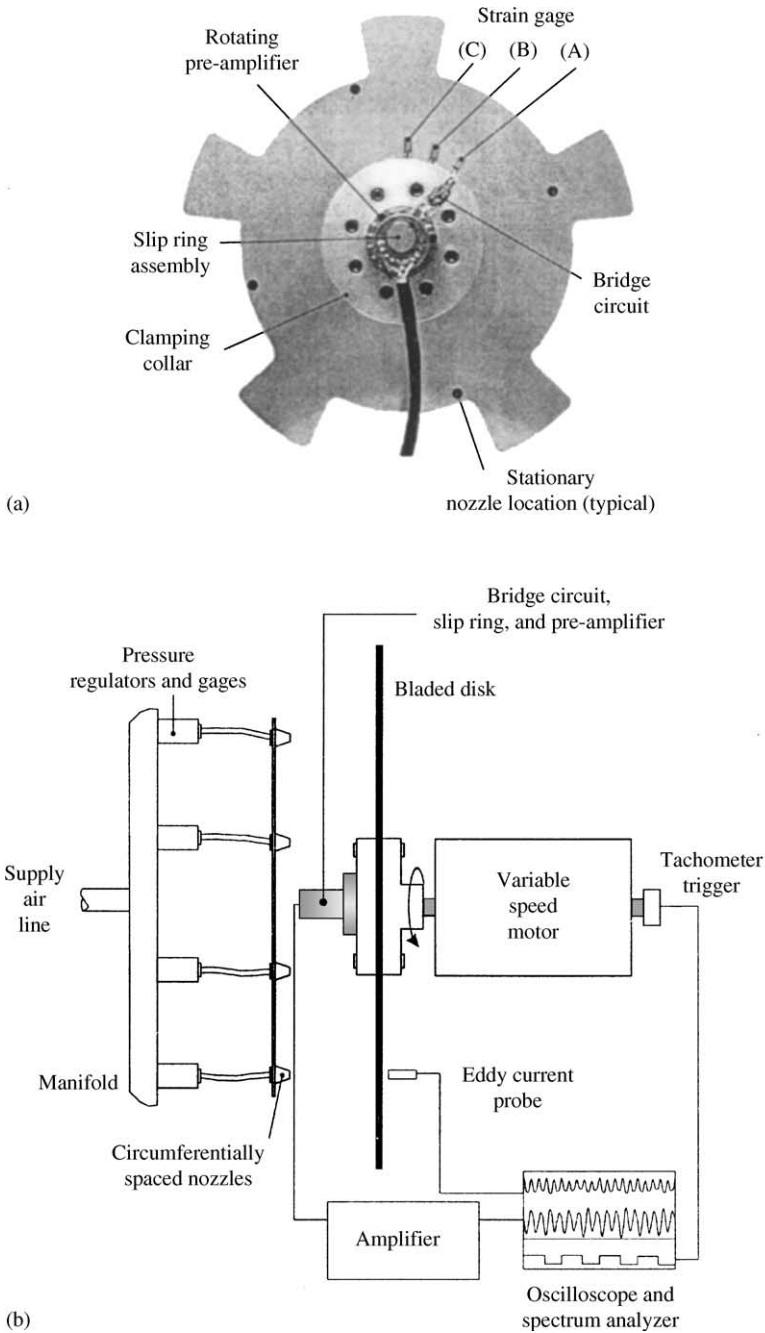


Figure 2. (a) Photograph of a typical bladed disk indicating strain gage locations, illustratively for the case $NB = 5$ and $N = 4$. (b) Schematic of the forced response spin test stand.

Point response measurements were made in the concentric $\chi^{(0)}$ and $\chi^{(1)}$ frames as labelled in Figure 1. In $\chi^{(0)}$, origin $\theta = 0$ is chosen so as to bisect a blade, and the two frames are related by $\phi = \theta + \Omega t$. In the air jet impingement measurements, a strain gage placed at one of the locations (A), (B), or (C) in Figure 2(a) was used to measure response in $\chi^{(0)}$.

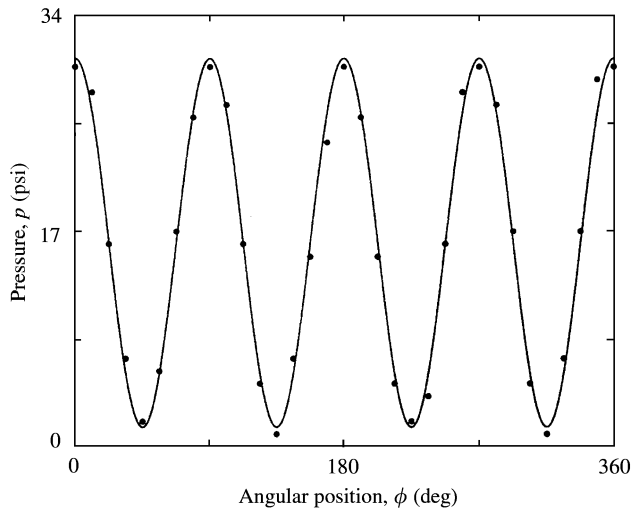


Figure 3. Measured (●) and least-squares cosine (—) pressure distributions at r^* near the bladed disk's surface with $N = 4$ evenly spaced nozzles at $\phi = 0, 90, 180,$ and 270° ; $P_0 = 30$ psi.

A Wheatstone quarter bridge circuit and a fixed-gain preamplifier were built on the rotating clamping collar in order to magnify the gage's signal prior to it crossing the slip ring assembly. This configuration is desirable to the extent that while noise is unavoidably introduced as a signal crosses the sliding contacts within a slip ring, such effects can be minimized by amplifying the response signal prior to the noise, of comparably smaller magnitude, being introduced. Signal filtering in this approach becomes unnecessary, an important attribute in what follows as spectral content of the response signals is examined. To measure displacement relative to the excitation's frame, an eddy current probe having linear range 1.3 mm was located directly opposite an air jet nozzle. Response measurements were thus made simultaneously in $\chi^{(0)}$ and $\chi^{(1)}$ and recorded on an oscilloscope or spectrum analyzer.

Figure 4 depicts typical measured strain and displacement time histories for steady state response when a repeated doublet mode, nominally having four nodal diameters but distorted by other wavenumbers, responds to fourth order excitation. The signals in Figure 4 were taken over four complete revolutions, and they were synchronized by the tachometer's trigger signal, the trace of which is shown as the upper element in Figure 4. The condition for near-resonance with the jets pressurized to $P_0 = 30$ psi (solid line type) was established by tuning the motor's speed such that the excitation frequency was in the vicinity of the desired mode's natural frequency and that the strain amplitude was at local maximum relative to the rotation rate, while recognizing that centripetal tensioning of the disk does shift the natural frequencies relative to the values measured while the disk is stationary. For comparison, the quiescent measurements in Figure 4 (dashed line type) were recorded with the air jets depressurized. The eddy current probe's signal in this instance reflects the disk's non-flatness, and only a small amount of noise relative to the $P_0 = 0$ response is present in the strain gage signal of Figure 4(b). The repeatability of measurements so obtained is depicted in Figure 5, where four cycles of the eddy current probe's and strain gage's signals are synchronized and overlaid across one rotation period. As in Figure 4, time histories are shown in Figure 5 for the case of the air jets being alternatively pressurized (solid line type) and depressurized (dashed line type).

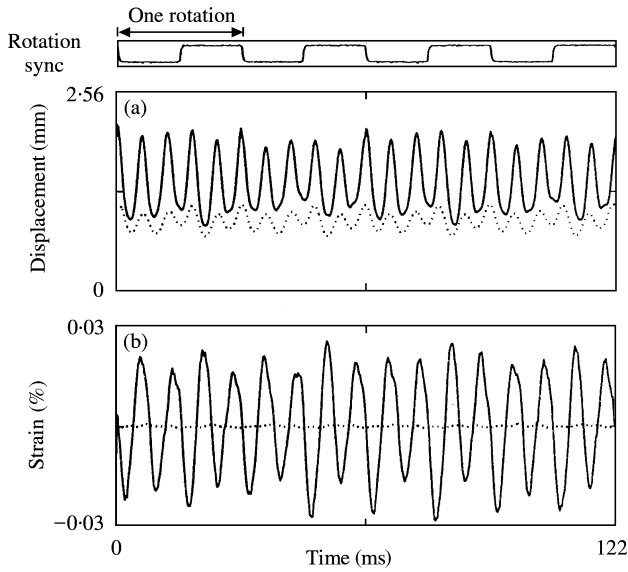


Figure 4. Measured forced response at $P_0 = 30$ psi (—), and the baseline quiescent signatures at $P_0 = 0$ (···), for the $P(0, 4)$ doublet mode in the (a) stationary $\chi^{(1)}$ and (b) rotating $\chi^{(0)}$ frames; strain gage (A), $N = 4$, $NB = 5$, $\Delta r = 4.76$ cm, and $\alpha = 40^\circ$. The tachometer synchronization signal is also shown over four revolutions to indicate the rotation rate.

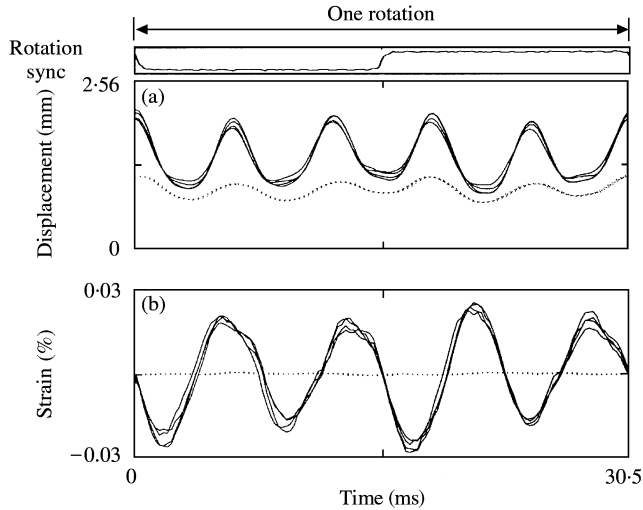


Figure 5. Superposition of four individual measurements of the forced response at $P_0 = 30$ psi (—), and the baseline quiescent signatures at $P_0 = 0$ psi (···), for the $P(0, 4)$ doublet mode in the (a) $\chi^{(1)}$ and (b) $\chi^{(0)}$ reference frames; strain gage (A), $N = 4$, $NB = 5$, $\Delta r = 4.76$ cm, and $\alpha = 40^\circ$. The tachometer synchronization signal is also shown over one revolution to indicate the rotation rate.

The measurement in Figure 5(a) at $P_0 = 0$ (dashed line type) is used to characterize the disk's non-flatness and the alignment imperfections associated with mounting the disk to its drive motor. To extract only the dynamic response over a signal revolution, the time histories at $P_0 = 0$ were averaged over four cycles so as to be indicative of disk runout alone, and they were then subtracted from the similarly averaged signals at $P_0 \neq 0$. The

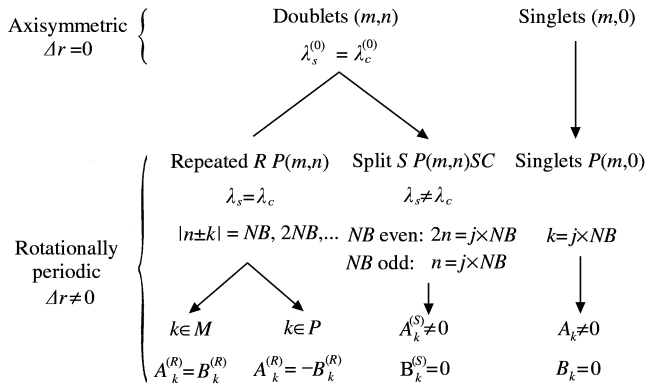


Figure 6. Natural frequency and mode structure for a certain class of rotationally periodic system.

response measurements depicted in Figures 12, 14–17, and 19, and discussed below, were developed in this manner.

3. NATURAL FREQUENCIES AND MODULATED MODE SHAPES

While forced response is the present focus, certain aspects of the structure’s free vibration are first discussed so as to better interpret the response calculations and measurements. As discussed in reference [25] for a certain class of rotationally periodic structures, the natural frequency and mode structure of the mock bladed disks is broadly classified according to the hierarchy of Figure 6.

In the limit of axisymmetry ($\Delta r \rightarrow 0$ in Figure 1), each doublet comprises members having even or odd symmetry in θ , and which are termed the cosine C and sine S components of repeated frequency $\omega_c^{(0)} = \omega_s^{(0)}$. Here, the superscript (0) denotes the base axisymmetric configuration, about which the structure is subsequently perturbed at $\Delta r \neq 0$. In Figure 6, the doublets are further classified as being either repeated R or split S pairs depending on the manner in which the frequencies transition upon perturbation. The notation $P(m, n)$ and $P(m, n) SC$ for the perturbed P repeated and split doublets, respectively, is used to distinguish the classical (m, n) modes having only nodal diameters and circles from those of the mock bladed disks. Attention is next placed on mode shape distortion through additional wavenumber content \mathcal{K} .

3.1. REPEATED DOUBLET

When $2n \neq j(NB)$ ($j = 1, 2, \dots$), the natural frequencies of the $P(m, n)$ doublet have the same value [14]. The corresponding mode shapes are expanded in the Fourier representations

$$U_{mnC}^{(R)}(r, \theta) = R_{mn}(r) \cos(n\theta) + \sum_{k \in \mathcal{K}} A_k^{(R)}(r) \cos(k\theta) \tag{2}$$

for the cosine component, and

$$U_{mnS}^{(R)}(r, \theta) = R_{mn}(r) \sin(n\theta) + \sum_{k \in \mathcal{K}} B_k^{(R)}(r) \sin(k\theta) \tag{3}$$

for the sine component, where $R_{mn}(r)$ is the mode’s radial dependence when the blades are not present. Set \mathcal{K} comprises the contamination wavenumber k which satisfy the criterion





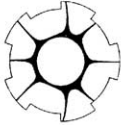

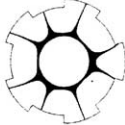



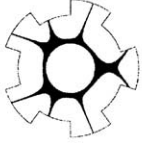

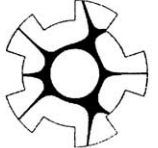



Δr (cm)	Sine component		Cosine component	
	Predicted	Measured	Predicted	Measured
0	 229 Hz	 225 Hz	 229 Hz	 227 Hz
1.91	 184 Hz	 180 Hz	 184 Hz	 183 Hz
3.81	 142 Hz	 140 Hz	 142 Hz	 141 Hz
4.76	 122 Hz	 118 Hz	 122 Hz	 120 Hz

Figure 7. Transition of nodal patterns and natural frequencies for the $P(0, 4)$ doublet as a function of increasing blade depth; $\alpha = 36^\circ$.

$|n \pm k| = NB, 2(NB), 3(NB), \dots$. Set \mathcal{K} is further broken down as $\mathcal{K} = \mathcal{M} \cup \mathcal{P}$, in which $\mathcal{M} = \{k : |n - k| = j(NB)\}$ (minus) and $\mathcal{P} = \{k : n + k = j(NB)\}$ (plus), where $j = 1, 2, \dots$ [25]. The coefficients in expansions (2)–(3) then satisfy the special relationships

$$A_k^{(R)}(r) = B_k^{(R)}(r), \quad k \in \mathcal{M}, \tag{4}$$

$$A_k^{(R)}(r) = -B_k^{(R)}(r), \quad k \in \mathcal{P}, \tag{5}$$

depending on the subset in which k lies.

As an example, the natural frequencies and mode shapes of experimental disks having five blades, $\alpha = 36^\circ$, and $\Delta r = 0, 1.91, 3.81, \text{ or } 4.76$ cm were examined. For this set, over the lower 10 modes, the natural frequency values measured through experimental modal analysis agreed in the aggregate within 5% with those predicted by companion finite-element models. To readily visualize the mode shapes and the distortion associated with wavenumber content \mathcal{K} , Chladni-type tests were conducted by placing piezoelectric actuators beneath the predicted anti-nodal positions. The bladed disk’s nodal patterns were rendered and photographed by gradually spreading $210 \mu\text{m}$ colored sand particles of mesh grade 65 as the actuators were driven in parallel at the particular mode’s natural frequency. For the $P(0, 4)$ doublet, Figure 7 depicts the frequency and mode shape results obtained

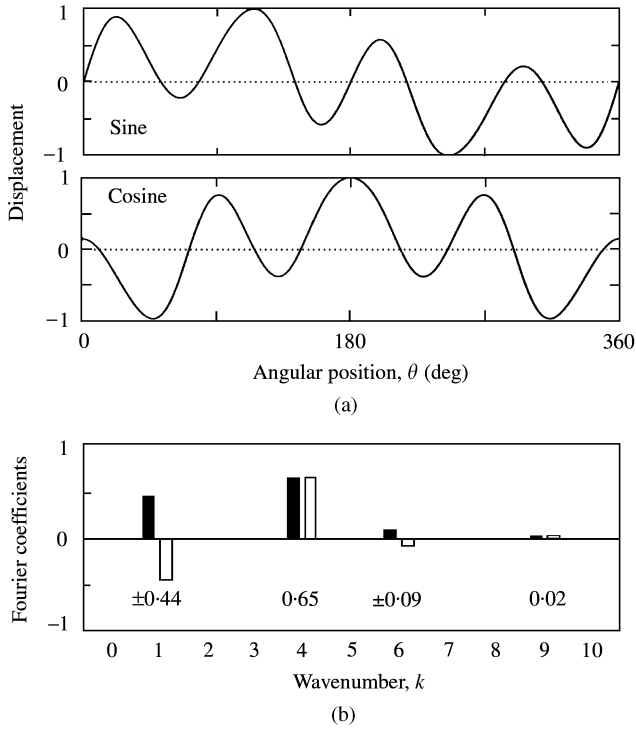


Figure 8. (a) Transverse displacements $U_{04S}^{(R)}$ and $U_{04C}^{(R)}$ for the $P(0, 4)$ doublet, and (b) Fourier coefficients $R_{04}^{(R)}$, $A_k^{(R)}$ (□), and $B_k^{(R)}$ (■) at $k = 1, 6,$ and 9 ; $NB = 5$, $\Delta r = 4.76$ cm, $r = 12.5$ cm, and $\alpha = 36^\circ$.

through finite element models of the four disks, and those obtained from the measurements as described. The shaded regions on each drawing or photograph denote the nodal lines. In principle, the natural frequencies of the S and C elements of $P(0, 4)$ are identical, but material inhomogeneity, residual stresses, geometric irregularity, and imperfect clamping contribute to the slight, several Hertz, difference in the so-called repeated frequencies. Further, mass loading of the sand slightly lowered and shifted the experimental frequencies.

While the nodal lines of $P(0, 4)$ are straight and oriented diametrically when $\Delta r = 0$, the nodal patterns in Figure 7 morph continuously as the blades are gradually introduced, and $U_{mnC}^{(R)}$ and $U_{mnS}^{(R)}$ become contaminated by \mathcal{H} . Figure 8 depicts the predicted displacements of the sine and cosine components in Figure 7 at $\Delta r = 4.76$ cm; here the displacements $U_{04C}^{(R)}$ and $U_{04S}^{(R)}$ are each normalized to unit peak amplitude. With $n = 4$ and $NB = 5$, this doublet suffers contamination in its wavenumber spectrum at $k = 1, 6, 9, 11, 14, 19, \dots$. In Figure 8(b), $A_k^{(R)}(r) = -B_k^{(R)}(r)$ for those wavenumbers $k = 1, 6, 11, \dots \in \mathcal{P}$, whereas $A_k^{(R)}(r) = B_k^{(R)}(r)$ for $k = 9, 14, 19, \dots \in \mathcal{M}$. In terms of the base n , subset \mathcal{M} , and subset \mathcal{P} components, the $P(0, 4)$ mode shapes evaluated at r^* become

$$\begin{aligned}
 U_{04C}^{(R)}(r^*, \theta) &= R_{04}(r^*) \cos(4\theta) + \sum_{k \in \mathcal{K}} A_k^{(R)}(r^*) \cos(k\theta) \\
 &= 0.65 \cos(4\theta) \\
 &\quad + \sum_{k \in \mathcal{P}} (-0.44 \cos(\theta) - 0.09 \cos(6\theta) + 0.01 \cos(11\theta) + \dots)
 \end{aligned}$$

$$+ \sum_{k \in \mathcal{H}} (0.02 \cos(9\theta) - 0.008 \cos(14\theta) + 0.0005 \cos(19\theta) + \dots), \tag{6}$$

$$\begin{aligned} U_{04S}^{(R)}(r^*, \theta) &= R_{04}(r^*) \sin(4\theta) + \sum_{k \in \mathcal{X}} B_k^{(R)}(r^*) \sin(k\theta) \\ &= 0.65 \sin(4\theta) \\ &\quad + \sum_{k \in \mathcal{P}} (0.44 \sin(\theta) + 0.09 \sin(6\theta) - 0.01 \sin(11\theta) + \dots) \\ &\quad + \sum_{k \in \mathcal{H}} (0.02 \sin(9\theta) - 0.008 \sin(14\theta) + 0.0005 \sin(19\theta) + \dots). \end{aligned} \tag{7}$$

As described in the sequel, the sign difference of the $A_k^{(R)}$ and $B_k^{(R)}$ coefficients has implication for setting the propagation direction of wave components in the response problem.

3.2. SPLIT DOUBLETS

When $n = j(NB)$ for $j = 1, 2, \dots$, the natural frequencies of a doublet mode split into distinct values, and the mode’s components are expressed

$$U_{mnC}^{(S)}(r, \theta) = R_{mn}(r) \cos(n\theta) + \sum_{k \in \mathcal{X}} A_k^{(S)}(r) \cos(k\theta), \tag{8}$$

$$U_{mnS}^{(S)}(r, \theta) = R_{mn}(r) \sin(n\theta), \tag{9}$$

where superscript (S) indicates that a split pair is considered.

Analogous to Figure 7, frequency splitting and migration of the $P(0, 5)SC$ mode shapes are shown in Figure 9 over four blade depths. In both the measured and predicted results, the nodal lines of the sine component remain straight and diametrically oriented at all Δr values, namely, $B_k^{(S)} = 0$. The split cosine mode, however, suffers contamination $A_k^{(S)} \neq 0$ at wavenumbers $k = 0, 10, 15, \dots$ as illustrated in Figure 10. For the baseline mock bladed disk, the mode shapes are given by

$$\begin{aligned} U_{05C}^{(S)}(r^*, \theta) &= R_{05}(r^*) \cos(5\theta) + \sum_{k \in \mathcal{X}} A_k^{(S)}(r^*) \cos(k\theta) \\ &= 0.39 \cos(5\theta) - (0.59 + 0.02 \cos(10\theta) + 0.006 \cos(15\theta) + \dots), \end{aligned} \tag{10}$$

$$U_{05S}^{(S)}(r^*, \theta) = R_{05}(r^*) \sin(5\theta) = 0.39 \sin(5\theta). \tag{11}$$

It is interesting to note that $P(0, 5)C$ has Fourier content identical to that expected for the perturbed singlet mode $P(1, 0)$ ($n = 0$ and $k = 5, 10, \dots$). The nodal pattern for $P(0, 5)C$ in Figure 9 transitions from being “nodal diameter-like” to “nodal circle-like” as Δr varies between 1.91 and 3.81 cm, and the converse behavior was observed in $P(1, 0)$.

4. REPEATED DOUBLET RESPONSE

When $N\Omega$ is at or near the natural frequencies $\omega_{mn}^{(R)}$ of a repeated doublet, and is well-separated from others in the spectrum, the bladed disk’s response is represented as a combination of the two members’ individual responses. By projecting p onto $U_{mnC}^{(R)}$ and $U_{mnS}^{(R)}$ and by using equations (4) and (5) with certain trigonometric identities, the response in $\chi^{(0)}$ becomes

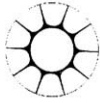

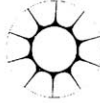

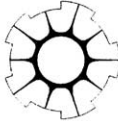

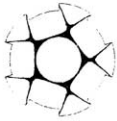
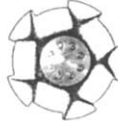


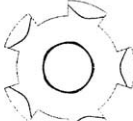



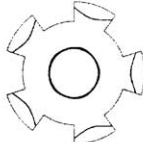

Δr (cm)	Sine component		Cosine component	
	Predicted	Measured	Predicted	Measured
0	 326 Hz	 322 Hz	 326 Hz	 324 Hz
1.91	 248 Hz	 242 Hz	 270 Hz	 269 Hz
3.81	 171 Hz	 168 Hz	 214 Hz	 214 Hz
4.76	 142 Hz	 140 Hz	 190 Hz	 187 Hz

Figure 9. Transition of nodal patterns and natural frequencies for the $P(0, 5)SC$ doublet as a function of increasing blade depth; $\alpha = 36^\circ$.

$$\begin{aligned}
 u_{mn}^{(R)}(r, \theta, t) &\approx q_{mnC}^{(R)}(t) U_{mnC}^{(R)} + q_{mnS}^{(R)}(t) U_{mnS}^{(R)} \\
 &\approx \left(\frac{a\pi P_0 R_{mn}(r^*)}{2(\omega^2 - \omega_{mn}^{(R)2})} \cos(\omega t) \right) U_{mnC}^{(R)} + \left(\frac{-a\pi P_0 R_{mn}(r^*)}{2(\omega^2 - \omega_{mn}^{(R)2})} \sin(\omega t) \right) U_{mnS}^{(R)} \\
 &\approx \frac{a\pi P_0 R_{mn}(r^*)}{2(\omega^2 - \omega_{mn}^{(R)2})} \times \left(R_{mn}(r) \cos(n\theta + \omega t) + \sum_{k \in \mathcal{H}} A_k^{(R)}(r) \cos(k\theta + \omega t) \right. \\
 &\quad \left. + \sum_{k \in \mathcal{P}} A_k^{(R)}(r) \cos(k\theta - \omega t) \right) \tag{12}
 \end{aligned}$$

for $N = n$, and

$$u_{mn}^{(R)}(r, \theta, t) \approx \left(\frac{a\pi P_0 A_N^{(R)}(r^*)}{2(\omega^2 - \omega_{mn}^{(R)2})} \cos(\omega t) \right) U_{mnC}^{(R)} + \left(\frac{-a\pi P_0 A_N^{(R)}(r^*)}{2(\omega^2 - \omega_{mn}^{(R)2})} \sin(\omega t) \right) U_{mnS}^{(R)} \tag{13}$$

for $N \in \mathcal{H}$. Here $q_{mnC}^{(R)}(t)$ and $q_{mnS}^{(R)}(t)$ are generalized co-ordinates for the cosine and sine components, and $u_{mn}^{(R)} = 0$ for all other N .

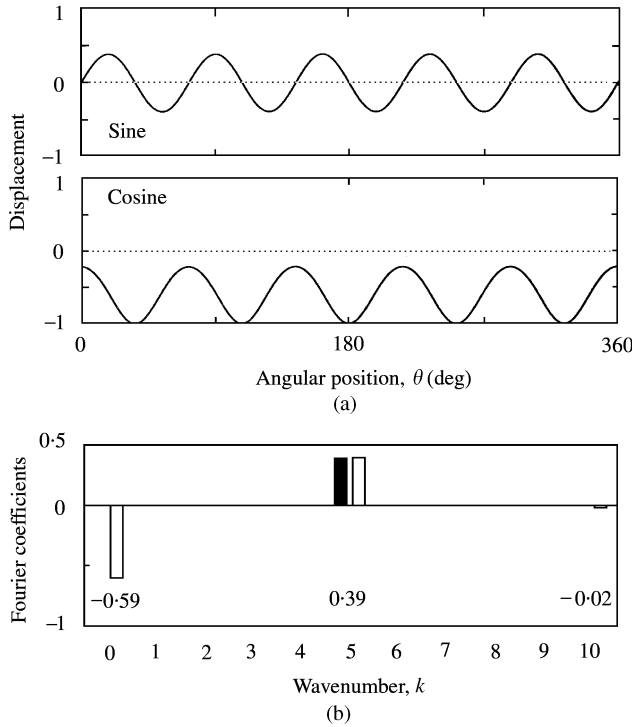


Figure 10. (a) Transverse displacements $U_{05S}^{(S)}$ and $U_{05C}^{(S)}$ for the $P(0, 5)$ SC doublet, and (b) Fourier coefficients R_{05} (■) and $A_k^{(R)}$ (□) at $k = 0$ and 10 ; $NB = 5$, $\Delta r = 4.76$ cm, $r = 12.5$ cm, and $\alpha = 36^\circ$.

4.1. CASE $N = n$

Consider the response of a disk to fourth order excitation with $NB = 5$, $\alpha = 40^\circ$, and $\Delta r = 4.76$ cm, which is set as the baseline system used in the response measurements below. The lower order Fourier coefficients at $r = r^*$ are $R_{04} = 0.64$, $A_1^{(R)} = -B_1^{(R)} = -0.46$, $A_6^{(R)} = -B_6^{(R)} = -0.12$, $A_9^{(R)} = B_9^{(R)} = 0.01$, and $A_{14}^{(R)} = B_{14}^{(R)} = 0.008$. Following substitution in equation (12), the steady state response becomes

$$\begin{aligned}
 u_{04}^{(R)}(r^*, \theta, t) \approx & \frac{0.32a\pi P_0}{(\omega^2 - \omega_{04}^{(R)2})} \times (0.64 \cos(4\theta + \omega t) \\
 & + \sum_{k \in \mathcal{M}} (0.01 \cos(9\theta + \omega t) - 0.008 \cos(14\theta + \omega t) \dots) \\
 & + \sum_{k \in \mathcal{P}} (-0.46 \cos(\theta - \omega t) - 0.12 \cos(6\theta - \omega t) + \dots)). \tag{14}
 \end{aligned}$$

This result is depicted graphically in Figure 11 over a time interval equalling one excitation period T or a quarter rotation. Because the Fourier coefficients n and $k \in \mathcal{M}$ have the same signs in this case, the corresponding wave components in Figure 11 and equation (14) travel in the same direction as p . However, due to their differing signs, components $k = 1, 6, \dots \in \mathcal{P}$ propagate counter-clockwise in Figure 1, opposite both the excitation and components $n = 4$ and \mathcal{M} .

As measured in Figure 5 by straining gage (A) and as in equation (14), the response in $\chi^{(0)}$ is harmonic and monofrequent at four times the rotation rate. The displacement as measured simultaneously with Figure 4(b) by the eddy current probe is depicted in Figure 12(a). This

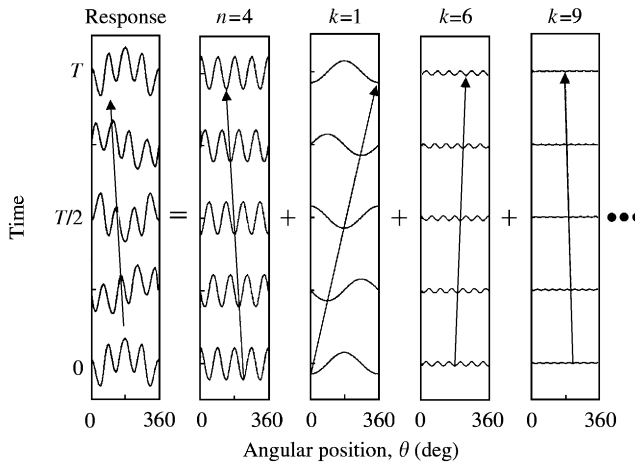


Figure 11. Steady state response in $\chi^{(0)}$ of the bladed disk's $P(0, 4)$ doublet over one excitation period, and its Fourier decomposition: $NB = 5$, $N = 4$, and $\alpha = 40^\circ$. Response components with the base $n = 4$ and contamination $k = 9 \in \mathcal{M}$ wavenumbers propagate backward with the excitation, while the contamination $k = 1$ and $6 \in \mathcal{P}$ waves propagate forward. The bold arrow in the figure's first element denotes the direction and rate of the excitation's propagation relative to the disk.

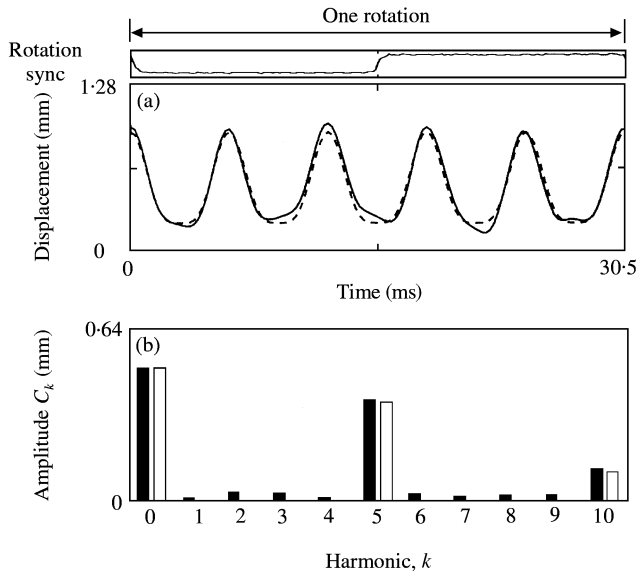


Figure 12. (a) Frequency response of the $P(0, 4)$ doublet in the $\chi^{(1)}$ reference frame, and (b) its Fourier content; $P_0 = 30$ psi, $NB = 5$, $N = 4$, $\alpha = 40^\circ$, $\phi = 0^\circ$, and $\Omega = 1967$ rev/min. The measured (— and ■), and the predicted (--- and □) response are shown. The tachometer synchronization signal is also shown over one revolution to indicate the rotation rate.

signature has dominant harmonics $k = 0, 5, 10, \dots$ with amplitudes $C_k = \sqrt{A_k^2 + B_k^2}$ calculated in Figure 12(b). The response of $P(0, 4)$ as observed in $\chi^{(1)}$ then becomes

$$\begin{aligned}
 u_{04}^{(R)}(r^*, \phi, t) \approx & \frac{0.32a\pi P_0}{(\omega^2 - \omega_{04}^{(R)2})} \times (0.64 \cos(4\phi) + 0.01 \cos(9\phi - 5\Omega t) - 0.008 \cos(14\phi - 10\Omega t) \\
 & - 0.46 \cos(\phi - 5\Omega t) - 0.12 \cos(6\phi - 10\Omega t) + \dots)
 \end{aligned} \tag{15}$$

through the substitution $\theta = \phi - \Omega t$ in equation (14). The response in $\chi^{(1)}$ as measured by the eddy current probe contains several harmonics, and the time record is correspondingly distorted in appearance. The base response wave component appears stationary in $\chi^{(1)}$. The $k = 1$ and 6 waves propagate opposite the excitation's direction and appear at frequencies 5Ω and 10Ω , respectively, in Figure 12. The $k = 9$ and 14 waves travel in the same direction as p and are also manifested as content at frequencies 5Ω and 10Ω . Each harmonic which contributes to the measured or predicted signals in $\chi^{(1)}$ generally develops from several propagating waves with amplitude depending on each component's wavenumber and propagation direction. In Figure 12, the predicted time record (dashed line type) and amplitudes (unshaded bars) are compared with the measured results, where the predicted C_0 has been scaled to match the measured value. Only small noise content is present at the harmonics 1–4 and 6–9.

4.2. CASE $N = k \in \mathcal{M}$

When the excitation order is commensurate with a wavenumber in \mathcal{M} , $A_N^{(R)}(r^*) = B_N^{(R)}(r^*)$ in equation (13), and the response becomes

$$u_{mn}^{(R)}(r, \theta, t) \approx \frac{a\pi P_0 A_N(r^*)}{2(\omega^2 - \omega_{mn}^{(R)2})} \times (R_{mn}(r) \cos(n\theta + \omega t) + \sum_{k \in \mathcal{M}} A_k^{(R)}(r) \cos(k\theta + \omega t) + \sum_{k \in \mathcal{P}} A_k^{(R)}(r) \cos(k\theta - \omega t)). \tag{16}$$

Here the response has the same general characteristics as for case $N = n$, and it differs only in that the amplitude becomes scaled by $A_N^{(R)}(r^*)$, and is substantially smaller than for the case $N = n$.

4.3. CASE $N = k \in \mathcal{P}$

Alternatively, when the excitation order lies in \mathcal{P} , $A_N^{(R)}(r^*) = -B_N^{(R)}(r^*)$. The response in $\chi^{(0)}$ is given by

$$u_{mn}^{(R)}(r, \theta, t) \approx \frac{a\pi P_0 A_N(r^*)}{2(\omega^2 - \omega_{mn}^{(R)2})} \times (R_{mn}(r) \cos(n\theta - \omega t) + \sum_{k \in \mathcal{M}} A_k^{(R)}(r) \cos(k\theta - \omega t) + \sum_{k \in \mathcal{P}} A_k^{(R)}(r) \cos(k\theta + \omega t)). \tag{17}$$

Further to the behaviour of the $P(0, 4)$ doublet in the baseline bladed disk, the response to sixth order excitation is

$$u_{04}^{(R)}(r^*, \theta, t) \approx \frac{-0.06a\pi P_0}{(\omega^2 - \omega_{04}^{(R)2})} \times (0.64 \cos(4\theta - \omega t) + \sum_{k \in \mathcal{M}} (0.01 \cos(9\theta - \omega t) - 0.008 \cos(14\theta - \omega t) \dots) + \sum_{k \in \mathcal{P}} (-0.46 \cos(\theta + \omega t) - 0.12 \cos(6\theta + \omega t) + \dots)), \tag{18}$$

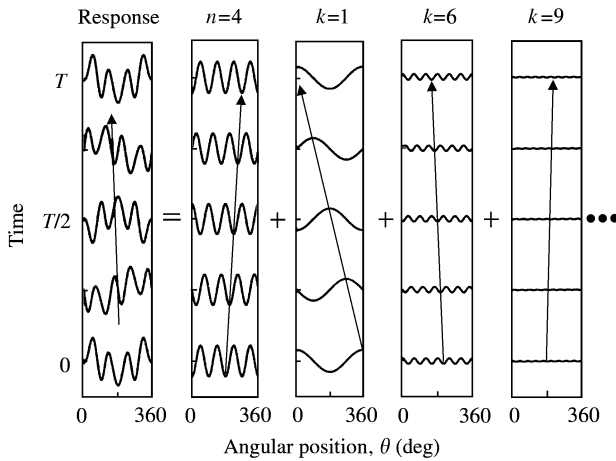


Figure 13. Steady state response in $\chi^{(0)}$ of the bladed disk's $P(0, 4)$ doublet over one excitation period, and its Fourier decomposition: $NB = 5$, $N = 6$, and $\alpha = 40^\circ$. Response components with the base $n = 4$ and contamination $k = 9 \in \mathcal{M}$ wavenumbers propagate forward, while the contamination $k = 1$ and $6 \in \mathcal{P}$ waves propagate backward with the excitation. The bold arrow in the figure's first element denotes the direction and rate of the excitation's propagation relative to the disk.

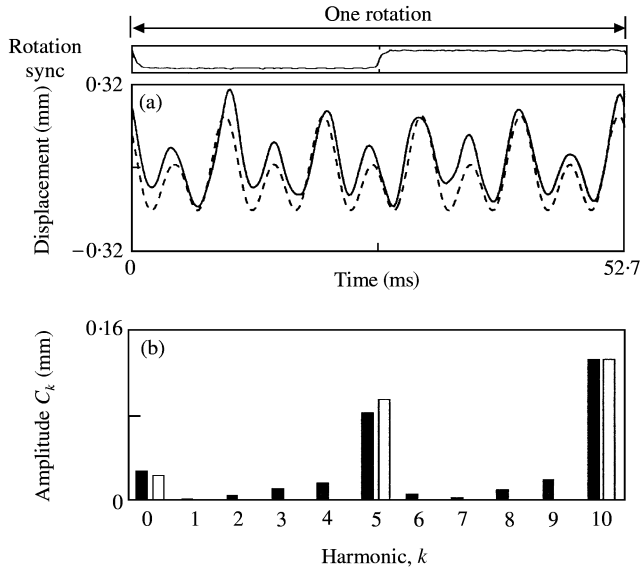


Figure 14. (a) Frequency response of the $P(0, 6)$ doublet in the $\chi^{(1)}$ reference frame, and (b) its Fourier content; $P_0 = 30$ psi, $NB = 5$, $N = 6$, $\alpha = 40^\circ$, $\phi = 0^\circ$, and $\Omega = 1149$ rev/min. The measured (— and ■), and the predicted (---- and □) responses are shown. The tachometer synchronization signal is also shown over one revolution to indicate the rotation rate.

where $\omega = 6\Omega$. This solution is represented in Figure 13. Response components at $k = 1, 6, \dots \in \mathcal{P}$ propagate with p , but the $n = 4$ and $k = 9, 14, \dots \in \mathcal{M}$ terms now travel opposite to it. The components superpose in the first element in Figure 13 so as to produce a deflection profile which is spatially modulated at each instant.

In experiments with the baseline bladed disk and a sixth order excitation, the fixed frame measurement of Figure 14 depicts frequency content at $0, 5\Omega$, and 10Ω . By scaling the

predicted C_{10} value to the measured one, the predicted and measured time records are compared in Figure 14(a). The measured amplitude ratios are $C_1/C_{10} = 0.21$ and $C_5/C_{10} = 0.63$, while the predicted ones are $C_1/C_{10} = 0.19$ and $C_5/C_{10} = 0.72$.

The time records and amplitudes in Figures 12 and 14 each change as the observer changes position ϕ in $\chi^{(1)}$. For instance, C_0 in Figure 12 vanishes in equation (15) at $\phi = (1 + 2j) \times 22.5^\circ$ ($j = 0, 1, 2, \dots$), namely, at the excitation's nodal positions. For $P(0, 4)$ driven by $N = 6$ in Figure 14, $C_0 = 0$ with observations at $\phi = (1 + 2j) \times 15^\circ$. Conversely, those amplitudes are maximized with the observer located at one of the excitation's anti-nodes.

5. SPLIT DOUBLET RESPONSE

5.1. CASE $N = n$

When driven by a travelling wave, the cosine and sine components of a split frequency doublet superpose in a manner similar to that of a repeated frequency doublet. Since the natural frequencies generally differ, however, the corresponding dynamic magnification factors for each mode component are not the same. When the excitation order equals the doublet's base wavenumber, and when ω is near the slightly separated natural frequencies, the steady state response in $\chi^{(0)}$ is expressed as

$$\begin{aligned} u_{mn}^{(S)}(r, \theta, t) &\approx q_{mnc}^{(S)}(t) U_{mnc}^{(S)} + q_{mns}^{(S)}(t) U_{mns}^{(S)} \\ &\approx \left(\frac{a\pi P_0 R_{mn}(r^*)}{2(\omega^2 - \omega_{mnc}^{(S)2})} \cos(\omega t) \right) U_{mnc}^{(S)} + \left(\frac{-a\pi P_0 R_{mn}(r^*)}{2(\omega^2 - \omega_{mns}^{(S)2})} \sin(\omega t) \right) U_{mns}^{(S)}, \end{aligned} \quad (19)$$

where $q_{mnc}^{(S)}(t)$ and $q_{mns}^{(S)}(t)$ are generalized co-ordinates for the split cosine and sine components respectively.

When ω is near $\omega_{mnc}^{(S)}$, the response in equation (19) is dominated by the cosine term, while the sine term dominates when $\omega \approx \omega_{mns}^{(S)}$. With reference to the $P(0, 5)$ SC doublet in the baseline bladed disk, when $\omega = 5\Omega$, the response forms as a nearly fifth-harmonic standing sine wave in $\chi^{(0)}$, with its nodal lines being fixed relative to the blades. In this case, the response measured by strain gage (B), which is placed at the response's anti-nodal position, is monofrequent at 5 times the rotation rate. The simultaneous fixed frame displacement measurement made by the eddy current probe is shown in Figure 15(a) where the time record also has harmonics at $k = 0$ and 10. The predicted and measured time records in Figure 15 are compared by scaling the predicted amplitude at $k = 10$ to the measured one. The zero and 10th harmonics in the fixed-frame measurement are best viewed in $\chi^{(1)}$ at the eddy current probe's location as

$$u_{05}^{(S)}(r^*, \phi = 0, t) \approx \frac{a\pi P_0 R_{05}^2(r^*)}{4(\omega^2 - \omega_{05s}^{(S)2})} (1 - \cos(10\Omega t)). \quad (20)$$

The predicted Fourier amplitude ratio here is $C_0/C_{10} = 1$, while the measured one in Figure 15 is 0.93. The harmonics $k = 1, \dots, 9$ are small and judged to be measurement noise.

When the excitation is instead set near $\omega_{mnc}^{(S)}$, the response as expressed in equation (19) is dominated by the cosine term. The response in $\chi^{(0)}$ is also monofrequent at 5 times the rotation rate. However, in this case, the response as measured by the eddy current probe over one disk rotation shown in Figure 16(a) becomes distorted by the presence of harmonics at $k = 5, 10, 15, \dots$ as depicted in Figure 16(b). The response in $\chi^{(1)}$ at the

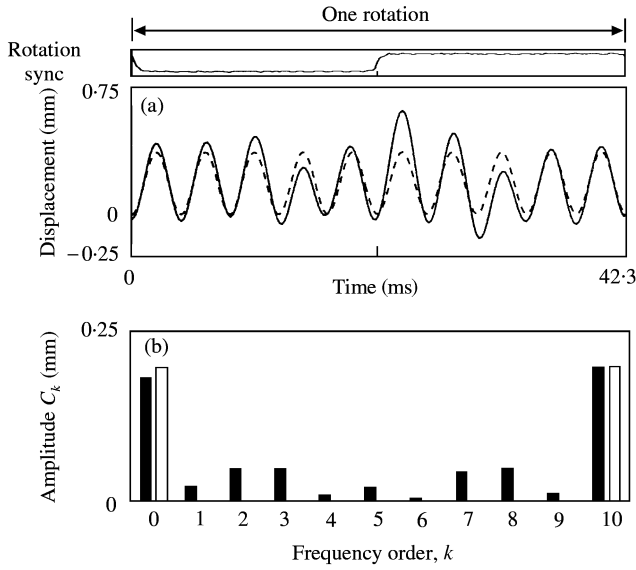


Figure 15. (a) Frequency response of the $P(0, 5)$ SC doublet driving at $P(0, 5)$ S component in the $\chi^{(1)}$ reference frame, and (b) its Fourier content: $P_0 = 15$ psi, $NB = 5$, $N = 5$, $\alpha = 40^\circ$, $\phi = 0^\circ$, and $\Omega = 1416$ rev/min. The measured (— and ■), and the predicted (---- and □) responses are shown. The tachometer synchronization signal is also shown over one revolution to indicate the rotation rate.

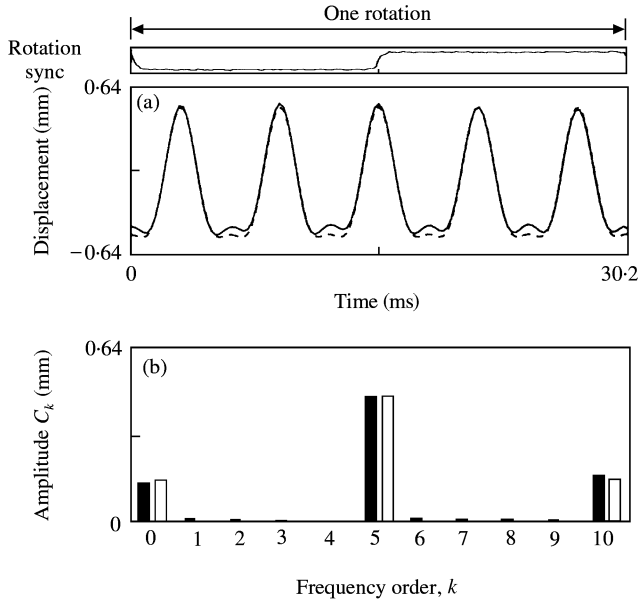


Figure 16. (a) Frequency response of the $P(0, 5)$ SC doublet driving at $P(0, 5)$ SC component in the $\chi^{(1)}$ reference frame, and (b) its Fourier content; $P_0 = 15$ psi, $NB = 5$, $N = 5$, $\alpha = 40^\circ$, $\phi = 0^\circ$, and $\Omega = 1990$ rev/min. The measured (— and ■), and the predicted (---- and □) responses are shown. The tachometer synchronization signal is also shown over one revolution to indicate the rotation rate.

probe's location is now expressed as

$$u_{05}^{(S)}(r^*, \phi = 0, t) \approx \frac{a\pi P_0 R_{05}^2(r^*)}{4(\omega^2 - \omega_{05c}^{(S)2})} (1 - 3 \cos(5\Omega t) + \cos(10\Omega t) - 0.06 \cos(15\Omega t) + \dots). \tag{21}$$

The magnitude of the fifth harmonic is expected to be some 3 times greater than those at $k = 0$ and 10. By scaling the predicted amplitude for the fifth harmonics to the measured value in Figure 16(b), the measured amplitude ratios are found to be $C_5/C_0 = 3.2$ and $C_5/C_{10} = 2.7$.

5.2. CASE $N = k \in \mathcal{K}$

When the excitation is at one of the contamination wavenumbers, the doublet's response in $\chi^{(0)}$ is approximated as

$$u_{mn}^{(S)}(r, \theta, t) \approx \left(\frac{a\pi P_0 A_N^{(S)}(r^*)}{2(\omega^2 - \omega_{mnC}^{(S)2})} \cos(\omega t) \right) U_{mnC}^{(S)}. \tag{22}$$

Here only $U_{mnC}^{(S)}$ responds to the excitation since $U_{mnS}^{(S)}$ contains no contamination harmonics, and the projection of p onto the split sine component vanishes. The response comprises cosine-oriented standing wave components at 5Ω . With amplitude now being scaled by $A_N^{(S)}(r^*)$, the response will be typically smaller than in the case $N = n$ at $\omega \approx \omega_{mnC}^{(S)}$.

6. SENSOR PLACEMENT OPTIMIZATION

In measuring a rotating structure's vibration with a view towards fatigue endurance, it is common practice to use such sensors as strain gages placed in the rotating reference frame. The objective is often to identify the peak displacement, strain, or stress that occurs in the structure. In the case of an axisymmetric structure driven by an N th order excitation, only the $n = N$ doublet mode is excited. The steady state response is a travelling wave at wavenumber N , and the response wave travels in the same direction and at the same phase speed as the excitation. At a given radial position, the vibration measurement made in $\chi^{(0)}$ at any circumferential position is identical in amplitude. In that case, the sensor can be placed at an arbitrary θ value on the disk, and the measurement is assured of providing the peak response when the time record is viewed over a full cycle.

In the present case, depending on the relation between N and \mathcal{K} , some response wave components propagate forward and some propagate backward with p ; the various components can propagate at different phase speeds; and they can have different magnitudes relative to one another. With that in mind, the treatment of optimal sensor placement in $\chi^{(1)}$ is revisited.

The general response of the $P(m, n)$ doublet in $\chi^{(0)}$ can be alternatively expressed as

$$\begin{aligned} u_{mn}^{(R)}(r, \theta, t) &\approx G(r^*) (U_{mnC}^{(R)}(r, \theta) \cos(\omega t) - U_{mnS}^{(R)}(r, \theta) \sin(\omega t)) \\ &\approx G(r^*) H(r, \theta) \cos(\omega t + \beta(r, \theta)), \end{aligned} \tag{23}$$

where $\beta = \tan^{-1} (U_{mnS}^{(R)}/U_{mnC}^{(R)})$ is a function of r and θ . Here

$$G = 0.5a\pi P_0 R_{mn}(r^*)/(\omega^2 - \omega_{mn}^{(R)2}), \quad N = n, \tag{24}$$

$$G = 0.5a\pi P_0 A_N^{(R)}(r^*)/(\omega^2 - \omega_{mn}^{(R)2}), \quad N \in \mathcal{K}. \tag{25}$$

Other factors being equal, the extrema of $u_{mn}^{(R)}$ depend on H , and by means of certain trigonometric identities, this quantity in equation (23) becomes

$$\begin{aligned} H^2(r, \theta^*) &= U_{mnC}^{(R)2}(r, \theta^*) + U_{mnS}^{(R)2}(r, \theta^*) \\ &= R_{mn}^2(r) + \sum_{k \in \mathcal{K}} A_k^{(R)2}(r) \\ &\quad + 2R_{mn}(r) \left(\sum_{k \in \mathcal{P}} A_k^{(R)}(r) \cos((n+k)\theta^*) + \sum_{k \in \mathcal{N}} A_k^{(R)}(r) \cos((n-k)\theta^*) \right), \end{aligned} \tag{26}$$

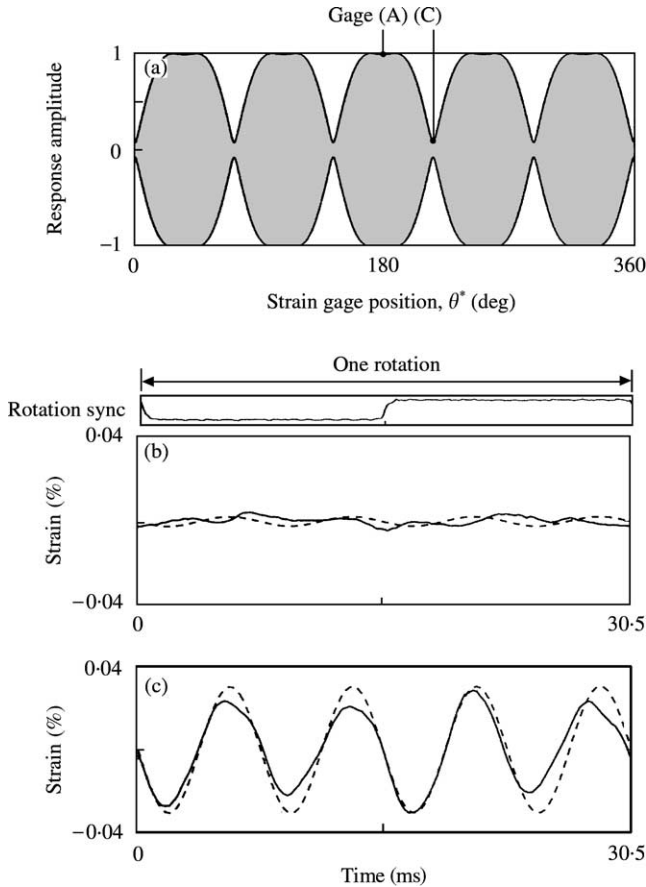


Figure 17. (a) Predicted range of response amplitude in $\chi^{(0)}$ of the $P(0, 4)$ doublet over one revolution, and response measurements with (b) strain gage (C) at $\theta = 216^\circ$, and (c) strain gage (A) at $\theta = 180^\circ$; $r = r^*$, $NB = 5$, $N = 4$, $\alpha = 40^\circ$, and $P_0 = 30$ psi: —; measured - - - -, predicted.

where θ^* denotes the sensor's location. Note that when the $A_k^{(R)}$ vanish in equation (26), the solution for an axisymmetric structure is recovered at $H = R_{mn}$ and $\beta = \tan^{-1}(n\theta)$ with $u_{mn}^{(R)} = G(r^*)H(r)\cos(\omega t + \beta)$. However, $H(r, \theta)$ changes character when periodic features are present, in which case the $A_k^{(R)}$ are generally non-zero. By setting $H_{,\theta} = 0$, the extrema of H occur at positions $\theta^* = j(360^\circ/2NB)$ where $j = 0, 1, 2, \dots, 2NB$. The maximum or minimum values of $H(r, \theta)$ can be determined only when specific values of R_{mn} and $A_k^{(R)}$ are provided in equation (26).

Considered the $P(0, 4)$ doublet in the baseline mock disk having sector angle $\alpha = 40^\circ$. In this case, $H^2(r^*, \theta^*) \approx 0.64(1 - 0.91 \cos(5\theta^*) - 0.24 \cos(10\theta^*))$. Five local minima exist for sensor placement at $\theta = j \times 72^\circ$, each of which also bisects a blade, and 10 maximal spots occur around $\theta = (j + 1) \times 36^\circ$. Figure 17(a) illustrates the range of $u_{04}^{(R)}(r^*, \theta^*)$ when the $P(0, 4)$ responds to $N = 4$ excitation.

The responses measured by strain gages (A) and (C), under identical operating conditions, are depicted in Figures 17(b) and 17(c), respectively. The predicted responses (dashed line type) are compared with the measured ones through scaling of the predicted amplitudes to the corresponding measured peak values. The predicted ratio of measured minimal ($\theta^* = 216^\circ$) to maximal ($\theta^* = 180^\circ$) response amplitude is approximately 6% in Figure 17(a), and the measured value is 11%.

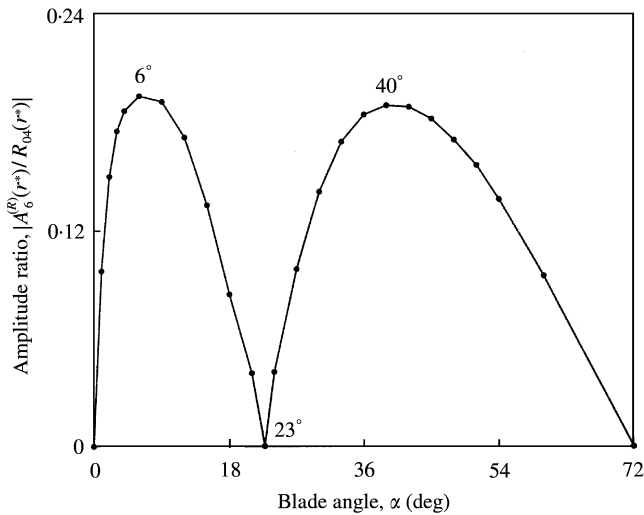


Figure 18. Magnitude of $A_6^{(R)}$ relative to R_{04} for the $P(0, 4)$ doublet shown as a function of blade sector angle α ; $Ar = 4.76$ cm, and $NB = 5$.

7. BLADE SPAN ANGLE

The presence of wavenumber content beyond n increases the potential for the bladed disk's response to travelling wave excitation sources, owing to the larger set of excitation orders which project onto the structure's mode shapes. In some cases, it is possible through re-design of the periodic features to reduce or even eliminate unwanted contamination, thereby reducing response amplitude.

As an example, Figure 18 depicts the magnitude of $A_6^{(R)}(r^*)$ in the baseline bladed disk's $P(0, 4)$ doublet as a function of blade span angle. Here, the magnitude is normalized with respect to $|R_{04}(r^*)|$. Coefficient $A_6^{(R)}$ has local maxima at $\alpha \approx 6^\circ$ and 40° . Further, the magnitude is zero near $\alpha = 23^\circ$. By choosing the span angle so as to reduce a particular harmonic, such as $k = 6$ here, the structure's forced response amplitude can likewise be minimized. Conversely, designs at 6° and 40° will have maximal response. Of course, in bladed-disk systems, aerodynamic and other concerns are important in setting the geometry, but it is interesting to note from the structural standpoint alone that re-design of the periodic features is one option for reducing wavenumber contamination. Figure 19 illustrates measured results associated with optimal tuning of α for $P(0, 4)$ being driven at sixth order. The strain measurement, for instance, at $\alpha = 23^\circ$ is reduced by some 85% relative to the value at $\alpha = 40^\circ$.

8. SUMMARY

The structure of modulated doublet modes in a mock flexible bladed disk was discussed through measurements, perturbation analysis, and finite element simulations. The steady state forced response of doublet modes as excited at various harmonic orders was investigated through measurements made simultaneously in the fixed and rotating reference frames. A repeated-frequency doublet mode was shown to respond when the excitation order matches either the base number of nodal diameters, or one of the contamination wavenumbers \mathcal{K} . Further, depending on the subset \mathcal{M} or \mathcal{P} in which N lies, the response can comprise wave components that travel either forward or backward, depending on

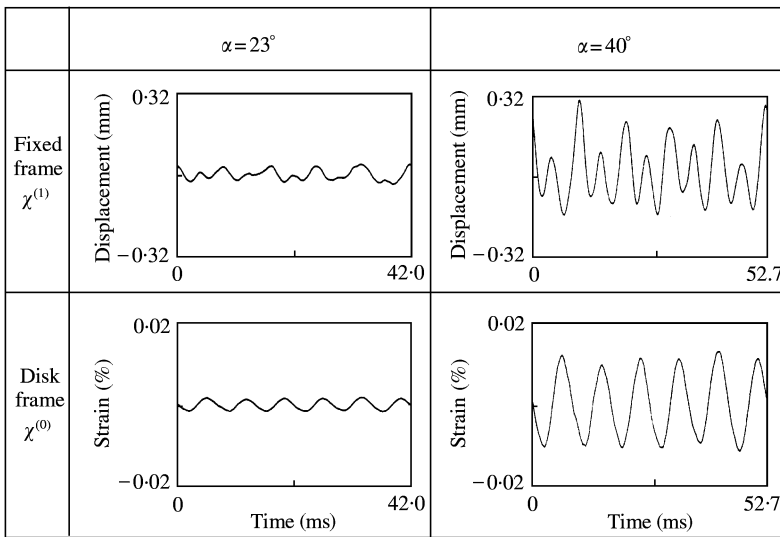


Figure 19. Comparison of the minimum ($\alpha = 23^\circ$) and maximum ($\alpha = 40^\circ$) measured responses of the $P(0, 4)$ doublet in fixed and rotating frames at r^* over one revolution; strain gage (A), $NF = 5$, $N = 6$, and $P_0 = 30$ psi.

satisfaction of certain algebraic relationships. These results are expected to have application to the vibration analysis, measurement, and design of various rotating machinery components, for which the present mock bladed-disk structure is a readily analyzed analog.

ACKNOWLEDGMENTS

This work was supported in part by the National Science Foundation and by AlliedSignal Incorporated, Aerospace Division.

REFERENCES

1. G. S. HAPPAWANA and O. D. I. NWOKAH 1998 *Journal of Sound and Vibration* **211**, 761–789. Free and forced response of mistuned linear cyclic systems: a singular perturbation approach.
2. J.-G. TSENG and J. A. WICKERT 1994 *American Society of Mechanical Engineers Journal of Vibration and Acoustics* **116**, 468–473. On the vibration of bolted plate and flange assemblies.
3. R. N. WAKE, J. S. BURDESS and J. T. EVANS 1998 *Journal of Sound and Vibration* **214**, 761–770. Changes in the natural frequencies of repeated mode pairs induced by cracks in a vibrating ring.
4. D. L. THOMAS 1974 *Journal of Sound and Vibration* **37**, 288–290. Standing waves in rotationally periodic structures.
5. D. L. THOMAS 1979 *International Journal for Numerical Methods in Engineering* **14**, 81–102. Dynamics of rotationally periodic structures.
6. G. X. REN and Z. C. ZHENG 1999 *Journal of Sound and Vibration* **225**, 597–610. Vibration characteristics of systems with multiple blades.
7. H. WANG and K. WILLIAMS 1995 *International Journal of Mechanical Systems and Signal Processing* **9**, 429–438. The vibrational analysis and experimental verification of a plane electrical machine stator model.
8. W. CAMPBELL 1924 *Transactions of the American Society of Mechanical Engineers* **46**, 31–160. The protection of steam-turbine disk wheels from axial vibration.
9. K. RAMESH, D. P. S. CHAUHAN and A. K. MALLIK 1997 *Journal of Sound and Vibration* **206**, 266–274. Free vibration of an annular plate with periodic radial cracks.
10. C.-H. HUANG and C.-C. MA 2000 *Journal of Sound and Vibration* **236**, 637–656. Vibration of cracked circular plates at resonance frequencies.

11. D. J. EWINS and M. IMREGUN 1984 *American Society of Mechanical Engineers Journal of Vibration, Acoustics, Stress, and Reliability in Design* **106**, 175–180. Vibration modes of packeted bladed disks.
12. C. H. J. FOX, R. S. HWANG and S. MCWILLIAM 1999 *Journal of Sound and Vibration* **220**, 517–539. The in-plane vibration of thin rings with in-plane profile vibrations. Part I: general background and theoretical formulation.
13. C. H. J. FOX, R. S. HWANG and S. MCWILLIAM 1999 *Journal of Sound and Vibration* **220**, 517–539. The in-plane vibration of thin rings with in-plane profile vibrations. Part II: application to nominally circular rings.
14. M. KIM, J. MOON and J. A. WICKERT 2000 *American Society of Mechanical Engineers Journal of Vibration and Acoustics* **122**, 62–68. Spatial modulation of repeated vibration modes in rotationally periodic structures.
15. S. A. TOBIAS and R. N. ARNOLD 1957 *Proceedings of the Institute for Mechanical Engineers*, 669–690. The influence of dynamical imperfection on the vibration of rotating disks.
16. S. C. HUANG and B. S. HSU 1992 *American Society of Mechanical Engineers Journal of Vibration and Acoustics* **114**, 468–476. Theory of receptance applied to modal analysis of a spinning disk with interior multi-point supports.
17. I. BUCHER and D. J. EWINS 1997 *International Journal of Mechanical Systems and Signal Processing* **11**, 577–601. Multidimensional decomposition of time-varying vibration response signals in rotating machinery.
18. D. J. EWINS 1969 *Journal of Sound and Vibration* **9**, 65–79. The effects of detuning upon the forced vibrations of bladed disks.
19. D. J. EWINS 1973 *Journal of Mechanical Engineering Science* **15**, 165–186. Vibration characteristics of bladed disc assemblies.
20. R. L. JAY, J. C. MACBAIN and D. W. BURNS 1984 *American Society of Mechanical Engineers Journal of Engineering for Gas Turbines and Power* **106**, 50–56. Structural response due to blade vane interaction.
21. F. KUSHNER 1980 *Journal of Mechanical Design* **102**, 579–548. Disc vibration—rotating blade and stationary vane interaction.
22. J. WILDHEIM 1981 *Journal of Sound and Vibration* **75**, 397–416. Excitation of rotating circumferentially periodic structures.
23. L. F. WAGNER and J. H. GRIFFIN 1996 *American Society of Mechanical Engineers Journal of Engineering for Gas Turbines and Power* **118**, 130–136. Forced harmonic response of grouped blade systems. Part I: discrete theory.
24. L. F. WAGNER and J. H. GRIFFIN 1996 *American Society of Mechanical Engineers Journal of Engineering for Gas Turbines and Power* **118**, 137–145. Forced harmonic response of grouped blade systems. Part II: application.
25. J. Y. CHANG and J. A. WICKERT *Journal of Sound and Vibration*, **242**, 69–83. Response of modulated doublet modes to travelling wave excitation.